

Aggressive Turn-Around Manoeuvres with an Agile Fixed-Wing UAV

Joshua M. Levin^{*} Meyer Nahon^{**} Aditya A. Paranjape^{***}

^{*} Mechanical Engineering Department, McGill University, Montreal, Canada (e-mail: joshua.levin@mail.mcgill.ca).

^{**} Mechanical Engineering Department, McGill University, Montreal, Canada (e-mail: meyer.nahon@mcgill.ca)

^{***} Department of Aerospace Engineering, IIT Bombay, Powai, Mumbai, India (e-mail: paranjape@aero.iitb.ac.in)

Abstract:

This paper investigates an aerobatic manoeuvre performed by an agile fixed-wing unmanned aerial vehicle, with the intent of determining how best the manoeuvre can be automated. The manoeuvre is an aggressive turn-around: a 180 degree reversal of the aircraft's heading, in which the space required for completing the turn is minimized. A comprehensive dynamics model of an agile fixed-wing aircraft is used to design trajectories of the manoeuvre off-line using optimal control. A methodology for evaluating the suitability of controllers for executing the manoeuvre is also presented.

© 2016, IFAC (International Federation of Automatic Control) Hosting by Elsevier Ltd. All rights reserved.

Keywords: Manoeuvrability, Agile Control, Aerospace Trajectories, Optimal Control, Optimal Trajectory, Optimality, Optimization Problems.



Fig. 1. Electrify by Great Planes Yak54 3D RC plane

1. INTRODUCTION

The use of unmanned aerial vehicles (UAVs) has grown dramatically over the past decade. While they were originally driven by military applications, they are now proposed for uses as diverse as detection and mapping of forest fires; monitoring of long distance power lines or pipelines in remote areas; aerial search and rescue; wildlife monitoring; road traffic monitoring; and police surveillance. Mainstream UAVs typically fall into one of two categories: fixed-wing or rotorcraft. Rotorcraft are usually chosen for tasks that make use of their ability to handle precisely at low speeds and stop mid-flight, however, they lack the endurance of fixed-wing aircraft. Advancements in research have begun to bridge the gap between these two categories of UAVs by increasing the agility of fixed-wing aircraft, and in so doing, broadening their suitability for missions requiring endurance *and* manoeuvrability.

Agile fixed-wing UAVs, one pictured in Figure 1, are capable of very impressive performance, as becomes evident when observing the extreme manoeuvres that can be performed by radio control (RC) pilots. Not only are these extreme manoeuvres spectacular, they are functionally

significant. For instance, avoiding obstacles in constrained environments - such as forests and urban areas - requires rapid transient motions. The manoeuvre of interest, an aggressive turn-around (ATA), finds its usefulness in re-treating from dead ends, among other applications. These capabilities, however, are rarely exploited by users of small UAVs due to the high complexity of piloting inputs that this entails - whether by a human teleoperator, or, even more so, by an automatic control system.

The study of the automation of aerobatic manoeuvres with fixed-wing UAVs is in its infancy. Most research in this area has focused on hovering and perching manoeuvres; see Green and Oh (2005), and Cory and Tedrake (2008). Little work, however, has been done to automate other agile manoeuvres. In Matsumoto et al. (2010), the authors designed a turn-around manoeuvre in which the aircraft first pulls its flight path angle up to nearly 90 degrees, then performs a 180 degree roll, drops its nose and recovers to level flight. The optimization problem they solved, and hence the manoeuvre, was restricted to two dimensions.

We approach the problem of automating an aggressive turn-around by investigating the dynamics of the manoeuvre, revealed in trajectories generated using optimal control theory, similar to the work of Cory and Tedrake (2007). Through this approach we are able to understand the full capabilities of the aircraft, and how closely a feedback controller can get the aircraft to those ultimate performance bounds.

The paper is organized as follows. Section 2 introduces the optimal control problem, presents the aircraft dynamics model, and discusses results. Section 3 reformulates the optimal control problem by introducing feedback control

laws and examines the results in comparison to those of Section 2.

2. OPTIMAL CONTROL

Trajectories were generated off-line by defining the ATA manoeuvre as the solution to an optimal control problem, which outputs the time histories of the motion variables and control inputs (thrust, and deflections in aileron, elevator, and rudder surfaces) throughout the manoeuvre.

2.1 Aircraft Dynamics Model

The aircraft dynamics model used in this paper was largely derived from the work of Khan (2016), which thoroughly models agile fixed-wing UAV dynamics over their full flight envelope. This work addresses all of the most relevant factors that influence an aircraft's flight behavior, namely: thruster dynamics, slipstream effects, and aerodynamics. Any deviations from this model were embraced in favor of computational efficiency during optimal control. The specific aircraft configuration used for this research is an Electrify by Great Planes Yak54 3D RC plane, seen in Figure 1. The mass, inertia, and geometric properties used in the model are attributed to this UAV.

The ordinary differential equations of motion for a rigid aircraft are as follows:

$$\begin{aligned}\dot{\mathbf{V}}_B &= \frac{1}{m}\mathbf{F}_B - \boldsymbol{\omega}_B^\times \mathbf{V}_B \\ \dot{\boldsymbol{\omega}}_B &= \mathbf{I}_B^{-1}[\mathbf{M}_B - \boldsymbol{\omega}_B^\times \mathbf{I}_B \boldsymbol{\omega}_B] \\ \dot{\mathbf{C}}_{BI} &= -\boldsymbol{\omega}_B^\times \mathbf{C}_{BI} \\ \dot{\mathbf{r}}_I &= \mathbf{C}_{BI}^\top \mathbf{V}_B\end{aligned}\quad (1)$$

where $\mathbf{V}_B = [u, v, w]^\top$ and $\boldsymbol{\omega}_B = [p, q, r]^\top$ are the translational and angular velocity of the aircraft resolved in the body frame, which is fixed to the aircraft and has origin at the aircraft's center of gravity. The inertia matrix, \mathbf{I}_B , is also resolved in the body frame, while the gravity and position vectors, \mathbf{g}_I and $\mathbf{r}_I = [x, y, z]^\top$, are resolved in the inertial frame. Note that:

$$\boldsymbol{\omega}_B^\times = \begin{bmatrix} 0 & -r & q \\ r & 0 & -p \\ -q & p & 0 \end{bmatrix}\quad (2)$$

The term \mathbf{C}_{BI} is the rotation matrix that parametrizes the attitude of the body frame relative to the inertial frame. It is composed of three rotations about the primary axes; roll, ϕ , about the x-axis, pitch, θ , about the y-axis, and yaw, ψ , about the z-axis:

$$\mathbf{C}_{BI} = \mathbf{C}_1(\phi)\mathbf{C}_2(\theta)\mathbf{C}_3(\psi)\quad (3)$$

The net forces and moments acting on the aircraft, \mathbf{F}_B and \mathbf{M}_B , have three sources: gravity, propulsion, and aerodynamics.

Thruster Model The effects of propulsion generated by the aircraft's thruster are accounted for in this portion of the model. The thruster model accepts three inputs:

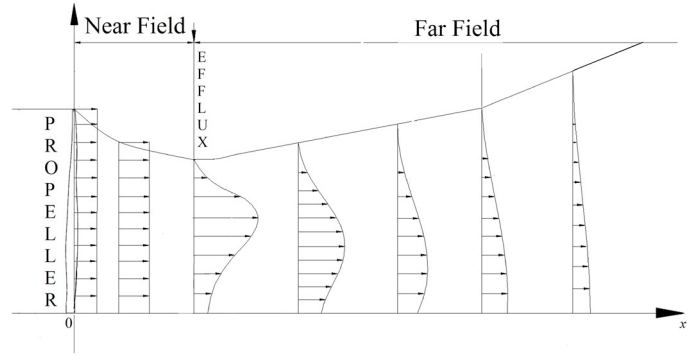


Fig. 2. Propeller slipstream: near field and far field regions

thrust, translational velocity, and angular velocity. It outputs the forces and moments, both aerodynamic and gyroscopic, created by the thruster unit (in the body frame), $\mathbf{F}_{B,T}$ and $\mathbf{M}_{B,T}$. Forces and moments are predicted under all flow conditions: static, axial, oblique, and reverse flow. All components of an electric-powered UAV thruster are considered, namely: the battery, electronic speed controller, brushless DC motor, and propeller. The velocity induced by the rotating propeller is also calculated for use in the slipstream model. The full details of the thruster dynamics - which are employed here in their entirety - are found in Khan and Nahon (2013).

Propeller Slipstream Model The propeller slipstream effect is a key component in the modeling of agile UAVs since it provides additional airflow over the control surfaces, which can be crucial in aggressive manoeuvring, especially at low speeds. The output of the slipstream model is the velocity of this additional airflow in the axial direction; the tangential and radial components are negligible. The axial airflow term is calculated differently for two regions: a near-field region and a far-field region, which are separated at the 'efflux plane', measured axially from the location of the propeller, as seen in Figure 2. The aircraft's fuselage and part of its main wing (that which is closest to the fuselage) reside in the near-field region. In this region the axial airflow's motion is dominated by the pressure force created by the propeller, which induces an acceleration. The airflow here is calculated using momentum theory, which is conventionally - and less accurately - used for representing the entire slipstream effect. The horizontal and vertical tail wings are located in the far-field region; this section of the model is both significant and novel. In this region, air viscosity and turbulence become more prominent and cause diffusion of the slipstream radially into the ambient flow. As a result of the momentum transfer between the fast-moving slipstream and the slow-moving ambient flow, the slipstream velocity decreases. In the far-field region, the slipstream velocity profile is calculated via a one-term Gaussian function to account for this diffusion phenomenon. The slipstream effect also includes a swirl component. This effect is modeled as a reduction of 60% on the thruster's reaction torque, \mathbf{M}_{B,T_x} . Refer to Khan and Nahon (2015) for a complete explanation of the slipstream model.

Aerodynamics Aerodynamic forces and moments are determined using a component breakdown approach that, in this paper, uses the following segments: starboard main

wing part one; starboard main wing part two; port main wing part one; port main wing part two; horizontal tail; vertical tail; and fuselage. Each side of the main wing is split into two segments (parts one and two): one inside and one outside of the propeller's slipstream. Each segment produces lift, drag, and a moment about its aerodynamic center. The velocity at each segment's aerodynamic center is calculated, in general as:

$$\mathbf{V} = \mathbf{V}_B + \boldsymbol{\omega}^\times \mathbf{r} + \mathbf{V}_s \quad (4)$$

where the position vector, $\mathbf{r} = [r_x, r_y, r_z]^\top$, measures from the aircraft's center of gravity to the aerodynamic center of the segment. This velocity vector is used to calculate the angle of attack on the segment:

$$\alpha_h = \arctan \frac{w}{u}, \quad \alpha_v = \arctan \frac{v}{u} \quad (5)$$

The term α_h applies to horizontal surfaces, and α_v to vertical surfaces. The aerodynamic forces and moments on each horizontal segment are calculated as:

$$\begin{aligned} \mathbf{F}_{B,seg} &= \frac{1}{2} \rho b c (V_x^2 + V_z^2) [CF_{x,seg} \quad 0 \quad CF_{z,seg}]^\top \\ \mathbf{M}_{B,seg} &= \frac{1}{2} \rho b c^2 (V_x^2 + V_z^2) [0 \quad C_{M,ac} \quad 0]^\top \end{aligned} \quad (6)$$

with analogous equations for the vertical segments. The values b and c are the span and mean aerodynamic chord of the segment, and ρ is the density of air. The force coefficients are obtained by resolving lift and drag coefficients, C_L and C_D , using the segment's angle-of-attack:

$$\begin{aligned} CF_{x,seg} &= C_L \sin \alpha_{h/v} - C_D \cos \alpha_{h/v} \\ CF_{y,seg} &= CF_{z,seg} = -C_L \cos \alpha_{h/v} - C_D \sin \alpha_{h/v} \end{aligned} \quad (7)$$

The forces and moments are transferred to the aircraft's center of gravity and summed to give the total aerodynamic forces and moments acting on the UAV:

$$\begin{aligned} \mathbf{F}_{B,aero} &= \sum \mathbf{F}_{B,seg} \\ \mathbf{M}_{B,aero} &= \sum (\mathbf{M}_{B,seg} + \mathbf{r}^\times \mathbf{F}_{B,seg}) \end{aligned} \quad (8)$$

The lift, drag, and moment coefficients, C_L , C_D , and $C_{M,ac}$, are calculated giving consideration to whether the segment is in a low-angle-of-attack or high-angle-of-attack regime. Effects of aspect ratio, stall, control surface deflection, bound vortices, and trailing vortices are all accounted for as detailed in Khan (2016). Finally, the net forces and moments acting on the aircraft are computed:

$$\begin{aligned} \mathbf{F}_B &= \mathbf{C}_{BIG} \mathbf{I} + \mathbf{F}_{B,aero} + \mathbf{F}_{B,T} \\ \mathbf{M}_B &= \mathbf{M}_{B,aero} + \mathbf{M}_{B,T} \end{aligned} \quad (9)$$

In addition to the equations of motion, Equation (1), the actuator dynamics of the control inputs - ailerons, elevators, rudder, and thrust - are modeled as follows, using the ailerons as an example:

$$\dot{\delta}_a = \frac{1}{\tau} (\delta_{ac} - \delta_a) \quad (10)$$

where τ is a time constant and δ_{ac} is the commanded deflection. The time constant of the first-order low pass filter equation that characterizes the actuator effectiveness was calculated based on experimentally verified servo rate limits.

2.2 Problem Formulation

Generating an ATA trajectory is posed as an optimal control problem for minimizing the weighted space inside which a heading change of 180 degrees is to be accomplished. The problem is constrained such that the aircraft must begin and return to straight and level flight. The optimal control problem is defined as follows:

$$\min J \triangleq \int_0^{t_f} (\eta_x x^2 + \eta_y y^2 + \eta_z z^2) dt \quad (11)$$

subject to the first-order dynamics of Equation (1),

the path constraints:

$$T \in [1000PW, 2000PW]$$

$$\begin{aligned} \delta_a &\in [-46^\circ, 46^\circ], \quad \delta_e \in [-34^\circ, 34^\circ], \quad \delta_r \in [-57^\circ, 57^\circ] \\ \psi &\in [-180^\circ, 180^\circ], \quad \theta \in (-90^\circ, 90^\circ), \quad \phi \in [-180^\circ, 180^\circ] \end{aligned}$$

and the boundary conditions:

$$\psi_{t_f} - \psi_0 \approx 180^\circ$$

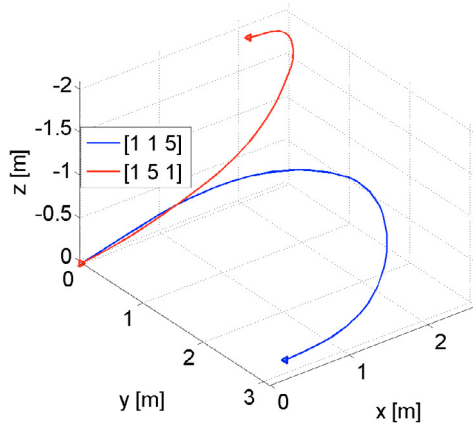
$$\gamma_0 \approx \beta_0 \approx \phi_0 \approx p_0 \approx q_0 \approx r_0 \approx 0$$

$$\gamma_{t_f} \approx \beta_{t_f} \approx \phi_{t_f} \approx p_{t_f} \approx q_{t_f} \approx r_{t_f} \approx 0$$

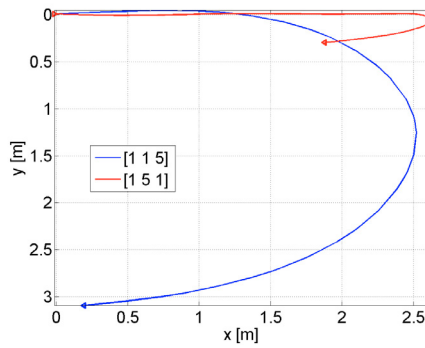
where the weights, η_x , η_y , and η_z , define the cost function to penalize the space of the manoeuvre. The boundary conditions on the flight path angle, γ , sideslip, β , and angular velocities in yaw (p), pitch (q), and roll (r), serve to define straight and level flight. The terminal time, t_f , is a free variable. The control surface deflections are modeled as angles, and the thrust as a pulse width (PW) modulated signal. The pulse width modulated signals, measured in microseconds, map approximately linearly to Newtons, where $1000PW \approx 0N$ and $2000PW \approx 10N$. This particular optimal control problem differs from Paranjape et al. (2013) in that the dynamic model is of 12th order and the control inputs are no longer the wind axis angles. Using a 12th order model, we generate a more complete picture of the aircraft dynamics, and are able to directly produce control input profiles for δ_e , δ_a , δ_r , and T . Note that these inputs are derived from a system with no feedback controller.

2.3 Results and Discussion

The optimal control problem was solved numerically using GPOPS-ii, Patterson and Rao (2014), which employs a variable-order adaptive orthogonal collocation method. Given the time it takes to generate trajectories (on the order of minutes) and the limited payload available on agile fixed-wing UAVs, we have no intent of implementing optimal control as an on-line trajectory generation method. Rather, the trajectories generated with this approach could be used as controller setpoints during flight.

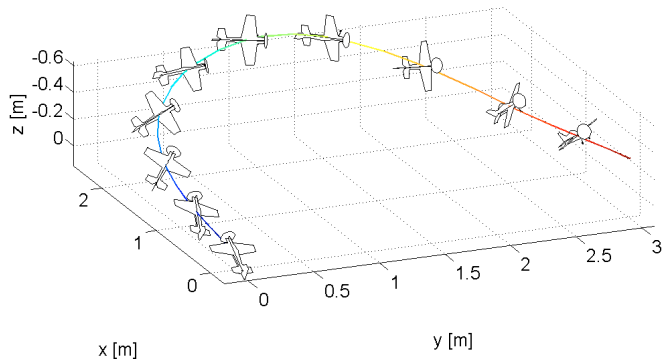


(a) Paths: displacements in x-y-z



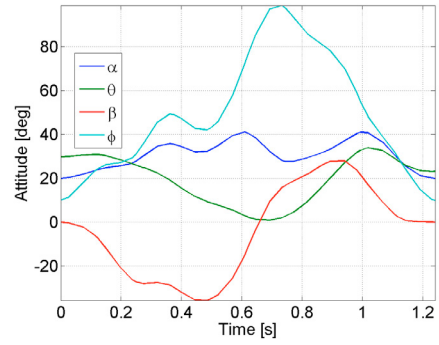
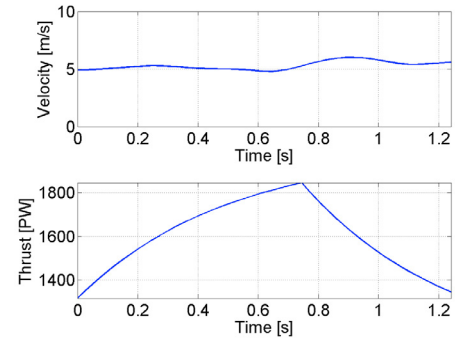
(b) Paths: displacements in x-y

Fig. 3. Paths resulting from different cost function weighting

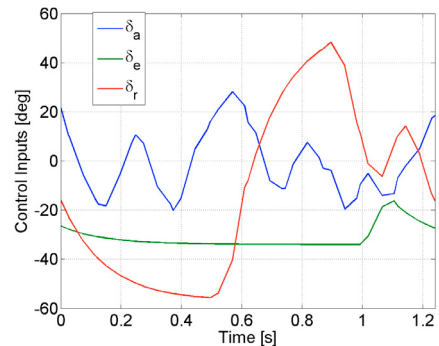
Fig. 4. 3D visualization of manoeuvre trajectory: displacements in x-y-z, $[\eta_x, \eta_y, \eta_z] = [1 \ 1 \ 5]$

The problem was assessed for various sets of cost function weights: η_x , η_y , and η_z to demonstrate their effect on the ATA path. Results are displayed in Figure 3 for two cases: $[\eta_x, \eta_y, \eta_z] = [1 \ 1 \ 5]$, which occurs over 1.24 seconds, and $[\eta_x, \eta_y, \eta_z] = [1 \ 5 \ 1]$, which occurs over 1.07 seconds. Notice how significantly the displacements in y and z depend on the weights. Depending on the specific purpose and requirements for performing an ATA, such as limited ground clearance, the cost function weights can be used to adjust the shape of the manoeuvre.

For the sake of clarity, the following discussion is limited to the case where $[\eta_x, \eta_y, \eta_z] = [1 \ 1 \ 5]$. A 3D visualization of the trajectory is provided by Figure 4. The line starting

(a) Attitude: angle-of-attack α , pitch θ , sideslip β , and roll ϕ over time

(b) Velocity and thrust over time

(c) Control surface deflections: ailerons δ_a , elevator δ_e , and rudder δ_r over timeFig. 5. Trajectory motion variables and control inputs, $[\eta_x, \eta_y, \eta_z] = [1 \ 1 \ 5]$

with blue and transitioning to red is aligned with the aircraft's translational velocity. Figure 5 depicts the aircraft's motion variables and control inputs throughout the ATA manoeuvre.

Figure 5a reveals many important characteristics describing the dynamics of the manoeuvre. The angle-of-attack is increased from the initial straight and level flight condition by approximately 10–20 degrees throughout the manoeuvre until it needs to recover to straight and level flight again. We also see in Figure 5a a negative sideslip throughout the first half of the manoeuvre. Using negative sideslip allows the aircraft to initiate the manoeuvre with its thrust pointed into the turn, producing a centripetal force. The second half of the turn utilizes positive sideslip. During this segment of the manoeuvre, the aircraft is banked at its highest roll angle of approximately 90 degrees, and is thus

deriving lift mainly from the fuselage, which is modeled as a flat plate. Therefore, a positive sideslip increases the angle-of-attack of the body, subsequently increasing lift to prevent the aircraft from losing significant altitude. The roll angle, ϕ , increases greatly to point the lift of the main wing in the direction of the turn, creating a side force. Notice as the roll angle decreases at the end of turn that the pitch angle, θ , rises back up to recover to level flight.

The thrust input increases steadily, also for approximately the first two thirds of the manoeuvre, and then descends at a similar rate, as is depicted in Figure 5b. The increase in thrust highlights its use in accelerating the aircraft in the direction of the turn, until it must descend back to a value used for straight and level flight. Also notice in Figure 5b that the velocity of the aircraft is relatively slow and barely changes throughout the ATA. Being able to perform high performance manoeuvres at low speeds is largely due to the increase of airflow over the wings created by the propeller slipstream. The increased airflow over the wings is what allows the control surfaces to maintain authority even as the aircraft's velocity is low.

Understanding the use of control surface deflections to execute the manoeuvre was also of interest. When we compare Figure 5c with Figure 5a we are able to deduce correlations between the control inputs and states. Until being needed to recover to straight and level flight, the elevator remains nearly saturated at its greatest negative value to increase the angle-of-attack. Large values of rudder deflection seem to induce the sideslip progression, while the ailerons, starting from a positive angle, fluctuate around trim condition to stabilize about the optimal roll profile.

3. OPTIMAL CONTROL WITH CONSIDERATION OF FEEDBACK CONTROLLER

The optimal control problem discussed in Section 2 considers only the aircraft's own dynamics while optimizing the ATA manoeuvre. In effect, this allows us to find the optimal ATA that the aircraft is physically capable of performing. However, since no feedback controller is embedded into the aircraft dynamics, we cannot claim that this level of performance will persist in automated flight. In this section we present a methodology for evaluating controllers by comparing their optimal trajectories to those of Section 2.

The purpose of this paper is not to delve into the details of feedback controller design, but rather to present a framework for evaluating their performance. It is clear that the design of the controller could be quite complex, and the need to resort to some form of non-linear control is foreseeable due to the transient nature of the state variables during the manoeuvre and the amount of cross-coupling between yaw and roll motion. However, for the purpose of demonstrating the effects of feedback control on performance, we chose to consider a combination of four single-input single-output (SISO) proportional-integral (PI) controllers: one channel controlling the elevator as a function of angle-of-attack; one channel controlling the aileron as a function of roll angle; one channel controlling the rudder as a function of sideslip angle; and a last channel controlling thrust as a function of speed.

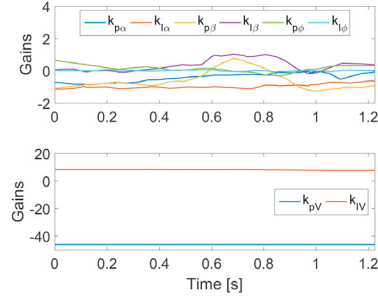


Fig. 6. Optimized proportional K_p and integral K_I gains for varying-gain controller, $[\eta_x, \eta_y, \eta_z] = [1 \ 1 \ 5]$

Table 1. Optimized proportional K_p and integral K_I gains for constant-gain controller, $[\eta_x, \eta_y, \eta_z] = [1 \ 1 \ 5]$

$k_{p\alpha}$	$k_{I\alpha}$	$k_{p\beta}$	$k_{I\beta}$	$k_{p\phi}$	$k_{I\phi}$	k_{pV}	k_{IV}
-0.64	-0.84	-0.83	0.94	0.36	0.01	-58	7.6

3.1 Control Laws and Problem Formulation

The controller consists of PI feedback terms. The feedback terms are one-to-one mappings between (a) α and δ_e ; (b) ϕ and δ_a ; (c) β and δ_r ; and (d) V and T . The control inputs, $\delta_{e,a,r}$ and T , thus become state variables. The elevator deflection, for instance, is found using:

$$\delta_e(t) = k_{p\alpha}(t)(\alpha_c(t) - \alpha(t)) + k_{I\alpha}(t) \int_0^t (\alpha_c(t) - \alpha(t))dt + \delta_{e_{trim}} \quad (12)$$

where $\alpha_c(t)$ is the commanded angle-of-attack. The gains k_p and k_I are also set as state variables, governed by the following dynamics:

$$\begin{aligned} \dot{k}_p &= \tilde{u}_p \\ \dot{k}_I &= \tilde{u}_I \end{aligned} \quad (13)$$

so that the optimization solves for $\alpha_c(t)$, $\tilde{u}_p(t)$, and $\tilde{u}_I(t)$ as the control inputs. The same procedure is followed for δ_a , δ_r , and T .

Two methods of optimally tuning the PI gains were investigated. In the first method, the gains k_p and k_I were optimized but constrained to be constant values by equating \tilde{u}_p and \tilde{u}_I to zero. In the other method, they were allowed to vary with time. The reason for conducting two methods of gain tuning was to compare how well a very simple, constant-gain PI controller would perform in contrast to one with varying gains. By allowing the gains to vary with time, we were also able to gain insight as to whether gain scheduling could be a viable strategy for performing optimal ATA manoeuvres.

3.2 Results and Discussion

The optimal control problem was again solved for each of the two SISO control policies: constant-gains and varying-gains. Figure 6 shows the optimized evolution of the gains when allowed to vary, and Table 1 lists the optimized constant-gains.

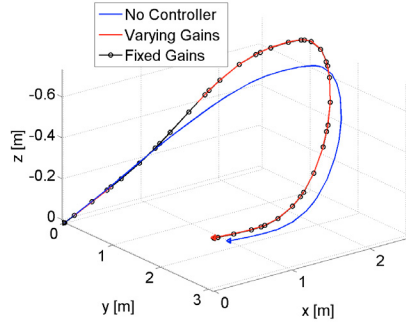


Fig. 7. Paths resulting from different controller setups: displacements in x-y-z, $[\eta_x, \eta_y, \eta_z] = [1 \ 1 \ 5]$

Table 2. Cost function values, $[\eta_x, \eta_y, \eta_z] = [1 \ 1 \ 5]$

No Controller	Varying-Gains	Constant-Gains
7.912	8.203	8.203

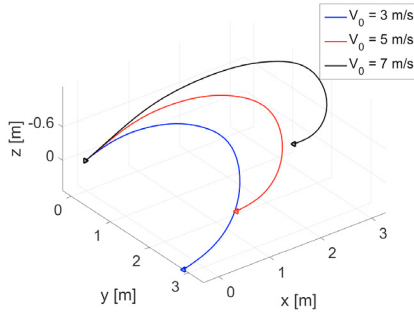


Fig. 8. Robustness of constant-gain controller: displacements in x-y-z, $[\eta_x, \eta_y, \eta_z] = [1 \ 1 \ 5]$

In Figure 7, the 3D paths are plotted for the case where $[\eta_x, \eta_y, \eta_z] = [1 \ 1 \ 5]$. Adding control laws to the aircraft dynamics is equivalent to further constraining the optimization problem. The cost function values, Table 2, act as a performance metric and confirm that the control laws slightly diminish performance. With that said, however, performance is practically equivalent between the two cases of control policies. This information aligns with the fact that the optimally varying-gains, Figure 6, remain practically constant, and nearly equivalent to the gains found in Table 1. While we were initially interested in investigating the merits of gain scheduling throughout a manoeuvre, these results show that this strategy may be superfluous for high performance ATA manoeuvres.

We were also concerned with evaluating robustness of the optimal gain profiles in terms of the initial conditions of the manoeuvre. This analysis focused only on the constant-gain case, which is more practically feasible and just as high performing as the case with varying gains. Since the manoeuvre, by definition, begins with straight and level flight, we parametrize the initial condition only by velocity. To evaluate robustness, we first generated a trajectory and the accompanying controller gains - as per Sec 3.1 - for an initial velocity of $V_0 = 5 \text{ ms}^{-1}$. Having developed a simulation in Simulink using the same dynamics model and controller, we then ran simulations for various initial velocities while maintaining the same gains and desired trajectory. Three resulting paths are displayed in Figure 8. The simulated aircraft was able to perform the ATA over a

wide range of initial velocities, spanning the breadth of its typical cruise speeds. While there remains to be a concrete guarantee of robustness, these results demonstrate the promise of a constant-gain PI controller to sufficiently control high-performance aggressive turn-around manoeuvres in the presence of uncertainties in initial conditions.

4. CONCLUSION

Future work will focus on improving the form of the controller. The methodology was developed such that it is readily able to be reformulated with different control laws.

ACKNOWLEDGEMENTS

The authors thank Waqas Khan for providing many parts of the agile fixed-wing UAV dynamics model.

REFERENCES

- Cory, R. and Tedrake, R. (2007). On the Controllability of Agile Fixed-Wing Flight. In *the Symposium on Flying Insects and Robots*.
- Cory, R. and Tedrake, R. (2008). Experiments in Fixed-Wing UAV Perching. In *the Guidance, Navigation, and Control Conference*, 1–12. AIAA.
- Green, W. and Oh, P. (2005). A MAV That Flies Like an Airplane and Hovers Like a Helicopter. In *the International Conference on Advanced Intelligent Mechatronics*, 693–698. IEEE.
- Khan, W. (2016). *Dynamics Modeling of Agile Fixed-Wing Unmanned Aerial Vehicles*. Ph.D. thesis, McGill University, Montreal, Quebec, Canada.
- Khan, W. and Nahon, M. (2013). Toward an Accurate Physics-Based UAV Thruster Model. *IEEE/ASME Transactions on Mechatronics*, 18(4), 1269–1279.
- Khan, W. and Nahon, M. (2015). Development and Validation of a Propeller Slipstream Model for Unmanned Aerial Vehicles. *Journal of Aircraft*.
- Matsumoto, T., Konno, A., Suzuki, R., Oosedo, A., Go, K., and Uchiyama, M. (2010). Agile Turnaround using Post-stall Maneuvers for Tail-sitter VTOL UAVs. 1612–1617. IEEE/RSJ.
- Paranjape, A., Meier, K., Shi, X., Chung, S., and Hutchinson, S. (2013). Motion Primitives and 3-D Path Planning for Fast Flight through a Forest. In *the International Conference on Intelligent Robots and Systems*, 2940–2947. IEEE.
- Patterson, M. and Rao, A. (2014). GPOPS-II: A MATLAB Software for Solving Multiple-phase Optimal Control Problems using HP-adaptive Gaussian Quadrature Collocation Methods and Sparse Nonlinear Programming. *ACM Transactions on Mathematical Software (TOMS)*, 41(1), 1.